nature communications

Article

https://doi.org/10.1038/s41467-025-61129-x

# Steering artificial photosynthesis via photoinduced conversion of monometallic to bimetallic sites in FeCo nitroprussides

Received: 15 June 2024

Accepted: 13 June 2025

Published online: 04 July 2025

Check for updates

Hao Wang[1,4], Gui-Lin Zhuang[2,4], Yingjie Fan[3,4], Hua-Qing Yin[1] ✉, Wei Zhang[2], Zhe Wu[1], Shuang Yao[1], Tong-Bu Lu[1], Wenbin Lin[3] ✉ & Zhi-Ming Zhang[1] ✉

Artificial photosynthesis provides an efficient strategy for solar energy storage via water splitting and $CO_2$ reduction, but it remains a challenge in tuning artificial photosynthesis between these two competing reactions. Herein, we demonstrate photoinduced conversion of monometallic to bimetallic sites in a Fe-Co nitroprusside (FeCo–NP) to steer the reaction path from $H_2$ evolution to $CO_2$ reduction. Monometallic Co sites achieve efficient $H_2$ production with 28.5 mmol $g^{-1}$ activity and 85.4% selectivity. Photoinduced release of nitrosyl groups from Fe sites generates bimetallic Fe-Co sites, which suppress $H_2$ evolution and enhance $CO_2$ reduction, yielding 31.5 mmol $g^{-1}$ activity and 87.3% selectivity for C1 products. Mechanistic investigations reveal that monometallic Co sites catalyze $H_2$ evolution via $H_2O$ adsorption and O-H cleavage while bimetallic Fe-Co sites facilitate both $H_2O$ and $CO_2$ adsorption and subsequent O and C hydrogenation for CO and HCOOH. This work uncovers a strategy to manipulate competing reaction pathways via photoinduced conversion of monometallic to bimetallic sites, which provides unique insights into addressing environmental issues and energy crises.

The global energy demand has been on the rise with the rapid development of modern society[1]. The increasing consumption of fossil fuels and emission of greenhouse gases have driven the urgent exploration of sustainable and renewable energy sources. Developing reliable energy sources and $CO_2$ conversion strategies toward a sustainable society represents an imperative strategy for solving environmental issues and energy crises[2]. Artificial photosynthesis harnesses renewable and abundant solar energy to achieve solar-to-chemical energy conversion via water splitting and $CO_2$ reduction reaction ($CO_2RR$), providing a potential pathway to mitigating the energy crisis and mitigate climate change[3–6]. Although significant efforts have been devoted to developing efficient catalysts for $CO_2RR$ and photocatalytic hydrogen evolution (PHE)[6–8], it remains a challenge to regulate these two competing reaction pathways in one catalytic system due to the involvement of multiple proton-coupled electron transfer (PCET) processes and reactive intermediates[9]. As catalytic activity and reaction pathways strongly depend on the intrinsic activities and microenvironments of active sites[10], catalytic systems with well-defined structures and synergistic active centers are needed to elucidate the key factors governing the selectivity for PHE and $CO_2RR$.

$CO_2RR$ requires the cleavage of high energy C=O bonds with multiple PCET processes[11–13]. As protons are needed for $CO_2$ reduction, PHE represents one key hurdle to achieving optimal $CO_2RR$ activity and selectivity. The selectivity for PHE and $CO_2RR$ has been altered by modulating the metal active sites and catalyst morphologies[14,15]. Dual-atom synergistic catalysis has recently provided a promising strategy

[1]Institute for New Energy Materials and Low Carbon Technologies, School of Materials Science & Engineering, State Key Laboratory of Crystal Materials, Tianjin University of Technology, Tianjin, China. [2]Institute of Industrial Catalysis, State Key Laboratory Breeding Base of Green-Chemical Synthesis Technology, College of Chemical Engineering, Zhejiang University of Technology, Hangzhou, China. [3]Department of Chemistry, The University of Chicago, Chicago, IL, USA. [4]These authors contributed equally: Hao Wang, Gui-Lin Zhuang, Yingjie Fan. ✉e-mail: hqyin@email.tjut.edu.cn; wenbinlin@uchicago.edu; zmzhang@email.tjut.edu.cn

to lower energy barriers for key reaction intermediates in $CO_2$RR and inhibit the competing PHE pathway[15–17]. For example, a series of diatomic catalysts were designed for $CO_2$RR to afford CO and HCOOH in high yields and selectivities[15–18]. Significant progress has been made in PHE using noble metal catalysts on various supports[4,19] and even earth-abundant transition metals[20,21]. Although many catalysts are now available for PHE and $CO_2$RR, most diatomic catalysts are difficult to synthesize, with particular difficulty in controlling their compositions and establishing their precise structures[18,22–26]. Straightforward methods are needed to control the occurrence of PHE and $CO_2$RR. However, inherent limitations of homogenous catalysts (catalyst deactivation via multimolecular pathways) and heterogeneous semiconductor catalysts (non-uniform catalytic sites and microenvironments) have prevented an in-depth investigation of their reaction paths and fundamental catalytic mechanisms[27,28]. It remains a challenge to tune the catalytic process from PHE to $CO_2$RR in a single catalytic system by inhibiting competing reactions.

The construction of synergistic catalytic sites in multi-metallic frameworks may provide an avenue for efficient regulation of PHE and $CO_2$RR and in-depth mechanistic studies. As a class of readily available crystalline materials with well-defined structures and tunable components[29], Prussian blue analogs (PBAs) have uniform catalytic centers for studying structure-performance relationships[30–32]. It remains a challenge to tune the catalytic process from PHE to $CO_2$RR by constructing different local microenvironments of active centers in PBAs under mild conditions. In this work, monometallic Co sites and Fe-Co bimetallic sites were precisely engineered by photo-induced release of nitrosyl groups in an Fe-Co nitroprusside (FeCo-NP), which was demonstrated as photoinduced conversion process. The photo-induced conversion of monometallic to bimetallic catalytic active sites in FeCo-NP further tuned the photosynthesis from PHE to $CO_2$RR. Single Co sites in FeCo-NP efficiently catalyzed water splitting with an $H_2$ yield of 28.5 mmol $g^{-1}$ and selectivity of 85.4%. The catalytic activity was changed to $CO_2$RR by generating Fe-Co bimetallic sites to achieve a total C1 (CO and HCOOH) yield of 31.5 mmol $g^{-1}$ and selectivity of 87.3%. Systematic investigations supported monometallic Co sites and bimetallic Fe-Co pairs as active catalysts for PHE and $CO_2$RR, respectively. This work provides insights into tuning the competing reaction paths of PHE and $CO_2$RR by regulating monometallic Co sites and bimetallic Fe-Co sites.

## Results

### Synthesis and characterization

FeCo-NP was synthesized on a 100-gram scale in aqueous solution at room temperature (25 °C, Supplementary Fig. 1), which improved its potential for real-world applications[30]. The pink FeCo-NP powder was irradiated to form FeCo-NP-n (Supplementary Fig. 2, $n = 2$, 6, 12, and 24, representing the irradiation time in hours). As shown in Supplementary Fig. 3, the color of these FeCo-NP-n materials gradually deepened with the increase of irradiation time. The color change suggests the change of metal coordination environments in FeCo-NP-n. Scanning electron microscopy (SEM) and transmission electron microscopy (TEM) showed that both FeCo-NP and FeCo-NP-24 exhibited a spherical morphology with an average diameter of 600 nm (Fig. 1b–c). High-resolution TEM (HRTEM) and energy-dispersive X-ray spectroscopy (EDS) elemental mapping images of FeCo-NP and FeCo-NP-24 confirmed their spherical morphology with a uniform distribution of N, Co and Fe (Fig. 1d and Supplementary Fig. 4). These results confirm the morphology integrity for FeCo-NP-24 after irradiation.

Powder X-ray diffraction (PXRD) studies demonstrated the maintenance of FeCo-NP-n crystallinity with different irradiation times (Fig. 2a). The diffraction peaks of FeCo-NP-n at 17.1°, 24.3°, 34.8° and 39.1° were assigned to the (200), (220), (400) and (420) planes, respectively, and matched those of the simulated PXRD pattern for FeCo-NP (CCDC 1730889). The C/N molar ratio increased from 0.83 in FeCo-NP to 0.99 in FeCo-NP-24, consistent with the calculated C/N ratio of 0.83 in FeCo-NP and 1.00 in FeCo-NP-24 (Supplementary Table 1). From the thermogravimetric analysis (TGA) curve (Supplementary Fig. 5), the weight loss of 17.1% below 130 °C was attributed to the loss of three water molecules (Calcd. 16.4%). Accordingly, the empirical formula of FeCo-NP was determined to be $Co[Fe(CN)_5NO]\cdot 3H_2O$. The TGA curve of FeCo-NP-24 showed a weight loss of 17.4% below 130 °C, corresponding to the weight loss of adsorbed water and coordinated water molecules (Calcd. 18.1% based on the assumed molecular formula of $Co[Fe(CN)_5H_2O]\cdot 2H_2O$) in FeCo-NP-24[33]. As the temperature increased, FeCo-NP showed 11.0% weight loss from 130 to 271 °C, which was attributed to the loss of all nitrosyl groups (Calcd. 9.1%) and partial loss of cyanide groups[34,35]. FeCo-NP-24 showed 9.0% weight loss from 130 to 283 °C, which was attributed to the loss of the weakly bonded axial CN group (Calcd. 8.7%)[34]. The reduced weight loss of FeCo-NP-24 supported the release of nitrosyl groups after 24 h pre-irradiation. FeCo-NP and FeCo-NP-24 experienced 49.1% and 42.5% weight losses, respectively, 130 to 870 °C, which are attributed to the loss of all organic groups. These weight losses are consistent with the calculated results based on the proposed molecular formulae of $Co[Fe(CN)_5NO]\cdot 3H_2O$ (Calcd. 48.9% for FeCo-NP) and $Co[Fe(CN)_5H_2O]\cdot 2H_2O$ (Calcd. 43.4% for FeCo-NP-24). These results support the loss of NO groups via 24 h irradiation of FeCo-NP. The TG-FTIR pattern of FeCo-NP showed ν(NO) and ν(CN) peak around 1900 $cm^{-1}$ and 2150 $cm^{-1}$ at 270 °C[36], respectively (Supplementary Fig. 6). In FeCo-NP-24, no ν(NO) peak was detected, which supports photoinduced release of nitrosyl groups (Supplementary Fig. 6).

The Fourier transform-infrared (FT-IR) spectrum of FeCo-NP showed a strong ν(NO) peak at 1941 $cm^{-1}$ and a strong ν(CN) signal at 2189 $cm^{-1}$(Fig. 2b)[37]. Upon irradiation, the ν(NO) peak at 1941 $cm^{-1}$ shifted gradually to 1946 $cm^{-1}$ and decreased in intensity over time. In situ FT-IR spectra also showed the same trend, proving the gradual release of NO groups under strong light irradiation (Supplementary Fig. 7). The ν(NO) peak nearly disappeared after 24 h irradiation, indicating photoinduced release of the nitrosyl groups from FeCo-NP to form pentacyanoferrate(II) sites in FeCo-NP-24. The nitrosyl group release caused a slight distortion of cyanide coordination and electron re-distribution, as evidenced by the shift of ν(CN) from 2189 $cm^{-1}$ to a broadened peak at 2089 $cm^{-1}$ gradually[38]. Both FeCo-NP and FeCo-NP-24 showed type-I nitrogen sorption isotherms with BET surface areas of 417.5 $m^2$ $g^{-1}$ and 768 $m^2$ $g^{-1}$, respectively, and micropore sizes of 0.69 nm and 1.14 nm, respectively (Fig. 2c, Supplementary Fig. 8). The increased surface area and pore size in FeCo-NP-24 support the maintenance of the crystalline framework and the loss of nitrosyl groups.

X-ray photoelectron spectroscopy (XPS) spectra showed the presence of Fe, Co, C, N and O before and after irradiation (Supplementary Fig. 9). FeCo-NP showed the characteristic N 1*s* peak at 403.3 eV for the nitrosyl group, but this peak disappeared in FeCo-NP-24, which supports photoinduced release of nitrosyl groups (Supplementary Fig. 10). FeCo-NP and FeCo-NP-24 showed N 1*s* peak at 398.6 and 398.2 eV, respectively, for the cyano groups. The 0.4 eV decrease in the $N_{CN}$ binding energy of FeCo-NP-24 is consistent the loss of the electron-withdrawing nitrosyl groups. Compared with FeCo-NP, FeCo-NP-24 did not show the characteristic O 1*s* signal for NO but exhibited a O 1*s* signal at 533.2 eV for $H_3^+O$ which provided charge balance for the framework (Supplementary Fig. 11)[39,40]. The presence of $H_3^+O$ was supported by pH decrease as the irradiation time increased (Supplementary Fig. 12). The Fe-$H_2O$ coordination behavior after nitrosyl group release was supported by the X-ray absorption near-edge structure (XANES) results and DFT calculations (see below). High-resolution XPS spectra of FeCo-NP showed Fe 2*p* peaks at 710.9 and 708.6 eV for $Fe^{2+}$ species (Fig. 2d)[37], which is consistent with the Mössbauer spectroscopy results (Supplementary Fig. 13 and Supplementary Table 2). The Fe 2*p* peaks remained essentially unchanged

https://doi.org/10.1038/s41467-025-61129-x

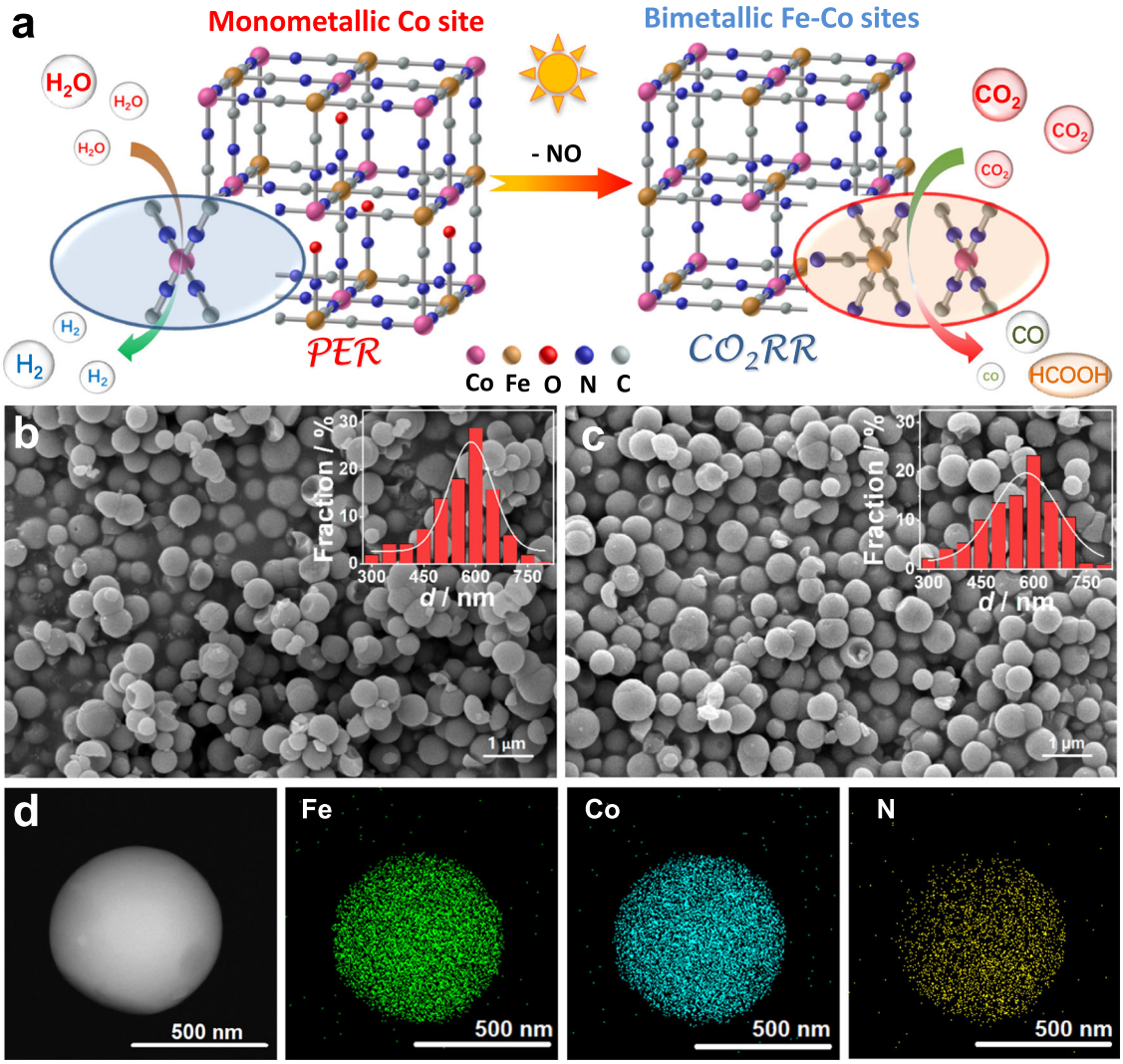


**Fig. 1 | Design of mono- and bi-metallic nitroprussides. a** Schematic illustration of photoinduced conversion of monometallic to bimetallic catalysts in the nitroprusside framework for PHE and $CO_2$RR, respectively. SEM images of **b** FeCo-NP and **c** FeCo-NP-24. The insets are particle size distribution of FeCo-NP and FeCo-NP-24, respectively. **d** EDS elemental mapping images of FeCo-NP-24. Source data for Fig. 1 are provided as a Source Data file.

after pre-irradiation (Fig. 2d). The broader Fe 2*p* peaks indicate the increased charge density on the Fe center after the nitrosyl release by pre-irradiation. The XPS spectra indicated the presence of $Co^{2+}$ species in both FeCo-NP and FeCo-NP-24 with Co $2p_{3/2}$ and Co $2p_{1/2}$ binding energies of 781.7/784.2 eV and 797.2/799.1 eV, respectively (Supplementary Fig. 14). Based on these results, we propose a formula of Co $[Fe(CN)_5H_2O]\cdot(H_3O)H_2O$ for FeCo-NP-24.

FeCo-NP and FeCo-NP-24 were further characterized by X-ray absorption spectroscopy (XAS) at the Fe and Co K-edge to determine their valance states and coordination environments. The near-edge features of Fe centers in FeCo-NP and FeCo-NP-24 appeared between those of Fe-foil and $Fe_2O_3$ and approached the position of $FeCl_2$ (Fig. 3a), indicating the +2 valence state for the Fe centers. The extended X-ray absorption fine structure (EXAFS) spectra of FeCo-NP and FeCo-NP-24 were fitted to experimental models to investigate the local coordination environments with reasonable R-factors and fitting parameters (Fig. 3b–d, Supplementary Figs. 15–16 and Supplementary Table 3). FeCo-NP exhibited five Fe-CN and one Fe-NO groups with Fe-N and Fe-C distances of 1.68 and 1.95 Å, respectively, in the first coordination shell (Fig. 3b–c and Supplementary Table 3). FeCo-NP-24 showed one axial and four planar Fe-CN groups with Fe-C distances of 1.95 and 2.07 Å, respectively, and a Fe-$OH_2$ group with an Fe-O distance of 2.22 Å in the first coordination shell (Fig. 3b and d). These results confirm the photoinduced release of nitrosyl groups[41,42]. Importantly, the absence of the Fe-Fe scattering path indicated the presence of isolated Fe centers without any aggregation in these catalysts (Supplementary Fig. 17). Two intensity maxima at 3.2 and 8.8 $Å^{-1}$ were observed in FeCo-NP EXAFS wavelet transform contour plots, which can be ascribed to the Fe-C and Fe-N bonds, respectively. In contrast, due to the loss of the nitrosyl group, two intensity maxima at 3.2 and 6.7 $Å^{-1}$ were observed in FeCo-NP-24 contour plots, which was ascribed to the Fe-C and Fe-O bonds. The XAS data further showed the presence of $Co^{2+}$ centers and the absence of Co-Co bonds in FeCo-NP-24 (Supplementary Figs. 18–19). These results support the presence of monometallic Co catalytic sites in FeCo-NP and Fe-Co bimetallic sites in FeCo-NP-24 (Supplementary Table 4).

## Photocatalytic investigation

FeCo-NP with monometallic Co active sites was transformed to FeCo-NP-24 with bimetallic Fe-Co sites via photoinduced nitrosyl group release (Fig. 4a and Supplementary Fig. 20). Photocatalytic $CO_2$RR and PHE experiments were performed to evaluate the different reactivity and selectivity of FeCo-NP and FeCo-NP-24. In the presence of photosensitizer (PS) $[Ru(bpy)_3]^{2+}$ and 1,3-dimethyl-2-phenyl-2,3-dihydro-

https://doi.org/10.1038/s41467-025-61129-x

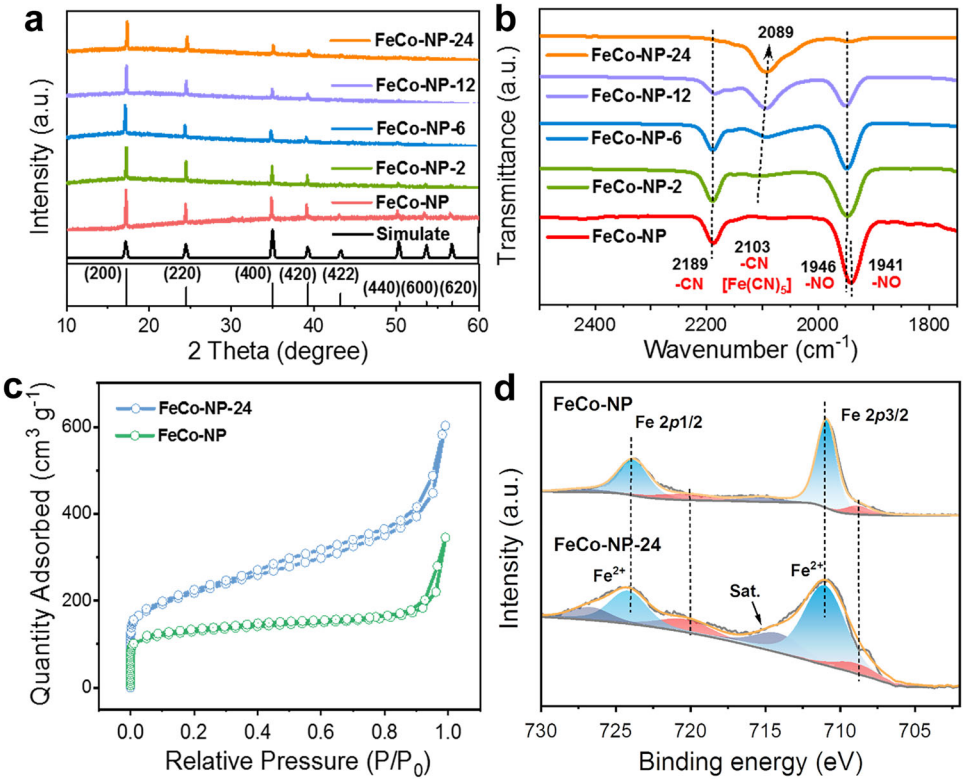


**Fig. 2 | Characterization of nitroprussides. a** PXRD patterns and **b** FT-IR spectra of FeCo-NP-n. **c** Nitrogen sorption isotherms of FeCo-NP and FeCo-NP-24, and **d** Fe 2*p* XPS spectra of FeCo-NP and FeCo-NP-24. Source data for Fig. 2 are provided as a Source Data file.

1H-benzo[d]imidazole (BIH), along with the irradiation time extension, the $H_2$ yield increased sharply with the C1 products generated slowly over FeCo-NP (Fig. 4b and Supplementary Fig. 21a). Interestingly, as the pre-irradiation time increased, the $CO_2$RR activity with FeCo-NP-n gradually increased, due to the loss of nitrosyl groups and the formation of bimetallic Fe-Co catalytic sites. In 4 h, FeCo-NP-24 achieved enhanced $CO_2$RR with a total yield of CO and formic acid of 31.5 mmol $g^{-1}$ and an 87.3% selectivity of C1 products (Fig. 4b and Supplementary Fig. 21b). These results demonstrated the ability to tune the photocatalytic activity from PHE to $CO_2$RR via photoinduced conversion of monometallic Co sites in FeCo-NP into bimetallic Fe-Co sites in FeCo-NP-24.

The catalytic activity of FeCo-NP-24 was well maintained in 5 cycles of photocatalytic $CO_2$RR (Fig. 4c). It is noteworthy that the PHE performance of FeCo-NP remained nearly unchanged after 5 cycles (Fig. 4d), indicating that no nitrosyl groups were released in FeCo-NP under the catalytic conditions with lower light irradiation intensity of 100 mW $cm^{-2}$ and in the presence of BIH. A control photocatalytic reaction at 200 mW $cm^{-2}$ showed gradually decreased PHE activity and increased $CO_2$RR activity (Supplementary Fig. 22). The characteristic peaks in the PXRD patterns of FeCo-NP and FeCo-NP-24 remained essentially unchanged after 5 cycles of photocatalysis (Supplementary Fig. 23). These results support the stability and reusability of FeCo-NP and FeCo-NP-24 catalysts during the photocatalytic reactions. In addition, photocatalytic performance tests were conducted using different amounts of FeCo-NP or FeCo-NP-24 (Supplementary Fig. 24). The catalytic activities of FeCo-NP and FeCo-NP-24 were approximately 30.5 mmol $g^{-1}$ for PHE and 30.0 mmol $g^{-1}$ for $CO_2$RR, respectively, and independent of the loadings of FeCo-NP and FeCo-NP-24 catalysts.

To support the role of bimetallic Fe-Co sites in FeCo-NP-24 in photocatalytic $CO_2$RR, we investigated the catalytic activity of $Co[Fe(CN)_5Im]$ (Im is imidazole) with Im coordination to the Fe sites (Supplementary Fig. 25)[43]. Similar to FeCo-NP, $Co[Fe(CN)_5Im]$ displayed a high PHE activity of 25.4 mmol $g^{-1}$ $H_2$ yield and a low $CO_2$RR activity of 6.9 mmol $g^{-1}$ C1 product yield. Replacing Co with Zn center, FeZn–NP displayed a much lower $CO_2$RR activity and showed no PHE activity (Supplementary Fig. 26). These results support the PHE activity of the monometallic Co sites and the $CO_2$RR activity of bimetallic Fe-Co sites.

The experiments conducted without PSs or in the dark exhibited no activity toward $CO_2$RR and PHE (Supplementary Table 5). The PS alone displayed a low activity of 0.87 mmol $g^{-1}$ $H_2$ and 3.42 mmol $g^{-1}$ C1 products. By increasing the $H_2O$ to $CH_3CN$ ratio from 0 to 1: 4, the $H_2$ yield increased from 0.16 mmol $g^{-1}$ to 30.10 mmol $g^{-1}$. Additionally, no C1 products were detected in the absence of $CO_2$, demonstrating that the C1 product was derived from the $CO_2$RR. These results demonstrate the photocatalytic activity of FeCo-NP for HER and FeCo-NP-24 for $CO_2$RR (Supplementary Fig. 27). Isotope-labeling experiments were conducted with $D_2O$ and in the $^{13}CO_2$ atmosphere to confirm the sources of hydrogen and carbon in the products, respectively. $D_2$ was detected in the photocatalytic reaction, demonstrating water as the proton source in the PHE process (Supplementary Fig. 28). When the photocatalytic experiments were performed in a $^{13}CO_2$-saturated system, $^{13}CO$ and $H^{13}COO^-$ were observed (Supplementary Figs. 29, 30), indicating that CO and HCOOH stemmed from photoreduction of $CO_2$. Finally, under Ar atmosphere, no CO was detected with FeCo-NP-24 as the catalyst, which further demonstrates the origin of CO in the $CO_2$ photoreduction system.

## Electrochemical study

The electron transfer pathway in the catalytic system was investigated by luminescence quenching of $[Ru(bpy)_3]^{2+}$ in the presence of BIH or catalyst (Supplementary Fig. 31). The Stern-Volmer quenching constant of $[Ru(bpy)_3]^{2+}$ by BIH is 4.9-folds higher than that by FeCo-NP-24. Moreover, as shown in Supplementary Fig. 32 and Supplementary

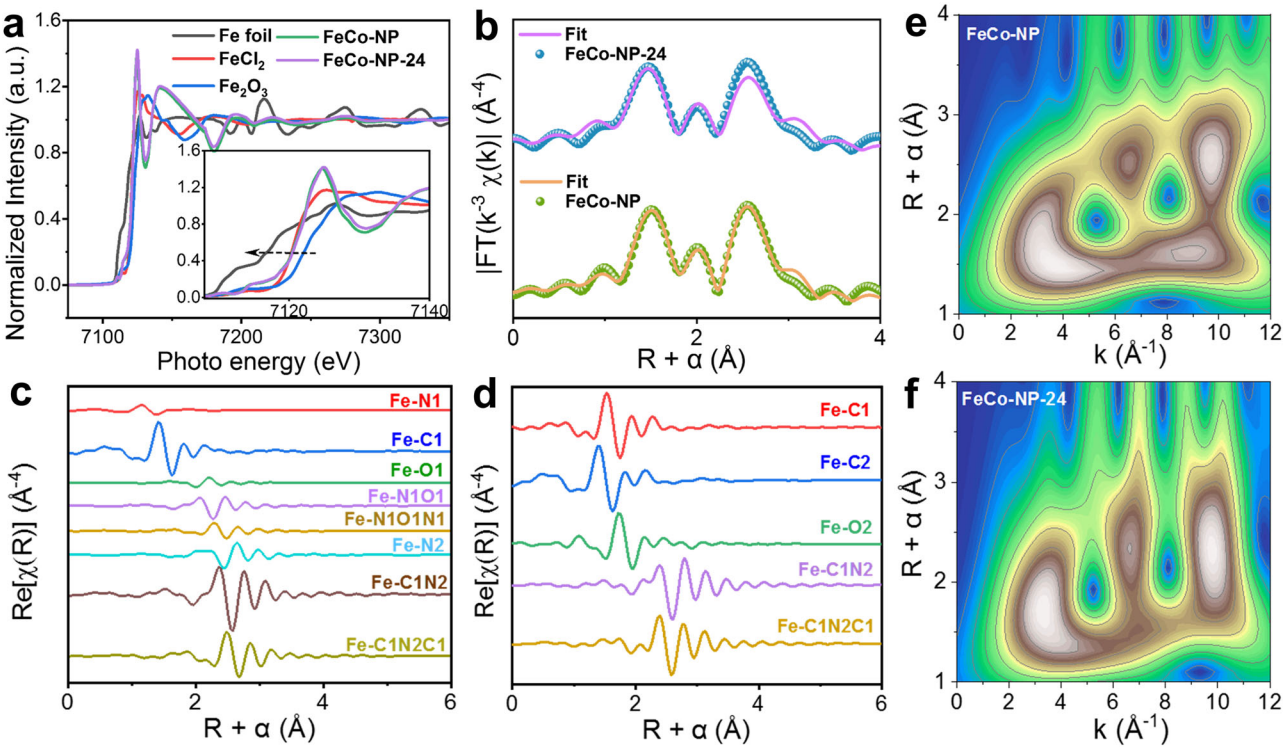


**Fig. 3 | XAS Characterization. a** Fe K-edge XANES spectra and the zoomed-in pre-edge spectra (The inset is a partial enlarged view.). **b** The Fe K-edge $k^3$-weighted Fourier transform (FT) and the fitting curves for FeCo-NP and FeCo-NP-24. The data are $k^3$-weighted and not phase-corrected. The real components curve fitting in R-spaces of **c** FeCo-NP and **d** FeCo-NP-24. Wavelet transforms $k^3$-weighted EXAFS spectra of **e** FeCo-NP and **f** FeCo-NP-24. Source data for Fig. 3 are provided as a Source Data file.

Table 6, from the cyclic voltammograms results, the oxidation potential of BIH was determined to be 1.06 V versus normal hydrogen electrode (NHE), more negative than the excited state reduction potential of $[Ru(bpy)_3]^{2+*}$ (1.18 V vs. NHE). These results supported the thermodynamic feasibility of the electron transfer from BIH to the excited PS $[Ru(bpy)_3]^{2+*}$ and obtaining $[Ru(bpy)_3]^{+}$. The reduction potential difference between reduced state $[Ru(bpy)_3]^{+}$ and FeCo-NP (−0.25 V) was larger than that of FeCo-NP-24 (−0.07 V), providing a larger driving force for electron transfer from $[Ru(bpy)_3]^{+}$ to FeCo-NP.

As shown in Supplementary Fig. 33, FeCo-NP-24 showed stronger absorption than FeCo-NP from 300 to 750 nm. The band gaps of FeCo-NP and FeCo-NP-24 were determined to be 1.61 and 1.51 eV, respectively. The flat-band potentials (FB) of FeCo-NP and FeCo-NP-24 were extrapolated to be −0.66 eV and −0.88 eV vs. NHE, respectively, from the Mott-Schottky plots (Supplementary Figs. 34–35). Hence, the valence band (VB) values of FeCo-NP and FeCo-NP-24 were calculated to be 0.95 eV and 0.63 eV, respectively. Thus, FeCo-NP and FeCo-NP-24 catalysts can drive the conversion of $CO_2$/CO (−0.53 V vs. NHE), $CO_2$/HCOOH (−0.61 V vs. NHE) and $H^+/H_2$ (−0.41 V vs. NHE).

Transient absorption spectra were investigated in degassing $CH_3CN$ to unveil the photocatalytic mechanism. As show in Supplementary Fig. 36, a bleaching signal around 455 and a positive peak around 380 nm were assigned to the ground state and triplet state absorption of $[Ru(bpy)_3]^{2+}$, respectively. In the presence of BIH, an absorption band at approximately 510 nm appeared, which was assigned to $[Ru(bpy)_3]^{+}$ absorption derived from the reductive electron transfer from BIH to the excited state $[Ru(bpy)_3]^{2+*}$. As shown in Fig. 5a and Supplementary Fig. 37, the lifetime of $[Ru(bpy)_3]^{2+}$ was determined as 0.79 μs and remained nearly unchanged at 0.73 μs and 0.76 μs with the addition of FeCo-NP or FeCo-NP-24, respectively, indicating no obvious electron transfer from $[Ru(bpy)_3]^{2+}$ to FeCo-NP or FeCo-NP-24 (Supplementary Fig. 36c and 37a). As shown in Fig. 5b, $[Ru(bpy)_3]^{+}$ formed with a lifetime of 69.30 μs after the reduction of $[Ru(bpy)_3]^{2+*}$ by BIH. Upon addition of FeCo-NP and FeCo-NP-24 with BIH, the lifetime of $[Ru(bpy)_3]^{+}$ was shortened to approximately 4.01 and 19.97 μs, respectively, implying efficient electron transfer from $[Ru(bpy)_3]^{+}$ to the catalyst and the regeneration of $[Ru(bpy)_3]^{2+}$ (Fig. 5b). The faster decay of $[Ru(bpy)_3]^{+}$ absorption in the presence of FeCo-NP suggests more efficient electron transfer from $[Ru(bpy)_3]^{+}$ to FeCo-NP over FeCo-NP-24. Based on these experiments, we propose the following mechanistic pathway (Supplementary Fig. 38). First, the $[Ru(bpy)_3]^{2+}$ is excited under the visible light irradiation to form $[Ru(bpy)_3]^{2+*}$, which accepts an electron from BIH to form $BI^+$ and $[Ru(bpy)_3]^{+}$. The $[Ru(bpy)_3]^{+}$ PSs efficiently donate electrons to the catalytic center to drive PHE and $CO_2$RR while regenerating $[Ru(bpy)_3]^{2+}$.

## Mechanism investigation

We next used in situ FT-IR spectroscopy to investigate the intermediates and products formed during photocatalytic $CO_2$RR and PHE. In FeCo-NP-24, the bidentate carbonate (b–$CO_3$*, 1588 $cm^{-1}$, * represents a reaction intermediate) and bicarbonate species ($HCO_3$*, 1637 $cm^{-1}$) were observed due to the adsorption and activation of $CO_2$ (Fig. 5c)[44,45]. The $CO_3$* and $HCO_3$* species were reduced to COO* by accepting electrons from the catalytic active centers, as evidenced by the appearance of $Fe^{2+}$-$COO^-$ intermediate (1560 $cm^{-1}$) and bridging carboxylates (1542 $cm^{-1}$)[46,47]. The $Fe^{2+}$-COOH species (1721 and 1674 $cm^{-1}$) and HCOO* species (1528 $cm^{-1}$) were also observed, likely generated via COO* reduction and hydrogenation. The COOH* and HCOO* species were further hydrogenated to form CO or HCOOH, respectively[48,49]. In addition, the C-H vibration absorption of H-COO* at 2950 $cm^{-1}$ correlated to the generation of formic acid (Supplementary Fig. 39). In contrast, the FeCo-NP system exhibited much lower bidentate carbonate (1589 $cm^{-1}$), bicarbonate (1638 $cm^{-1}$), and bridging

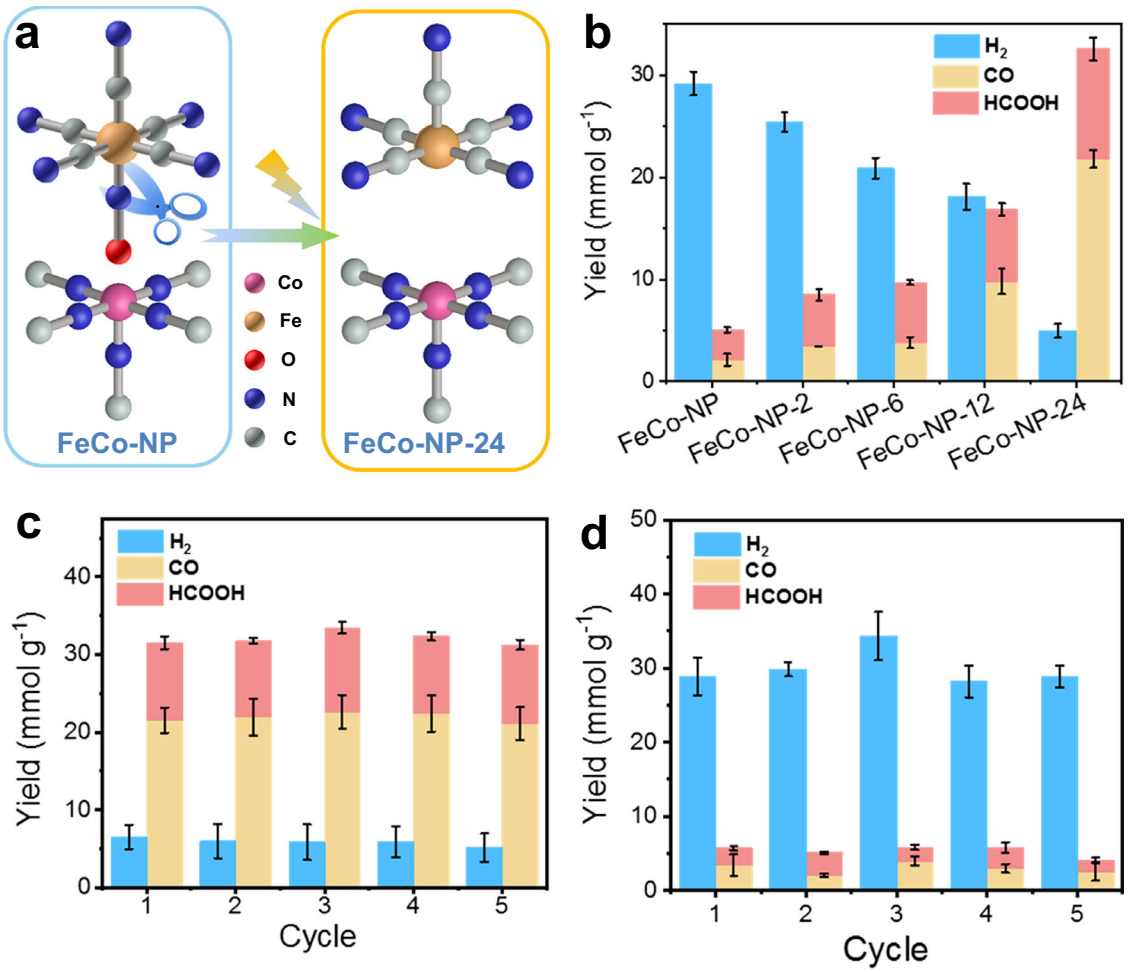


**Fig. 4 | Structural transformation and photocatalytic performance. a** Schematic illustration of nitrosyl group release via light irradiation. **b** Catalytic performance of FeCo-NP-n. **c** Recycle and catalyst stability of FeCo-NP-24 in photocatalytic $CO_2$RR. The error bars (standard deviation) in the Fig. 4a–d were obtained from three replicate experiments. **d** Recycle and catalyst stability of FeCo-NP in photocatalytic PHE. Photocatalytic experiments were performed in $CO_2$-saturated $H_2O/CH_3CN$ solution (v: v = 1: 9) at room temperature (25 °C). Source data for Fig. 4 are provided as a Source Data file.

carboxylate (1542 $cm^{-1}$) signals, consistent with lower $CO_2$ adsorption and CO/HCOOH yields (Fig. 5d)[47,49]. Moreover, the absence of significant dissociative $CO_3^{2-}/HCO_3^-$ vibrational signatures at 1620/2080 $cm^{-1}$ demonstrated that $HCO_3$* and $CO_3$* species were not generated through pH fluctuations during the water-splitting process (Fig. 5 and Supplementary Fig. 39)[50]. Based on the in situ Raman spectroscopic analysis, the evolution of vibrational signatures at $HCO_3$* (1006 $cm^{-1}$), b-$CO_3$* (1026 $cm^{-1}$), OCO* (1127 $cm^{-1}$), and COO* (1395 $cm^{-1}$) over time under varying pH conditions were documented, demonstrating the $CO_2$-activated intermediates come from the electron transfer mechanism from $CO_3$*/$HCO_3$* to form COO* intermediates (Supplementary Fig. 40). In addition, the absence of dissociative $CO_3^{2-}$ species excluded the reaction pathways involving $CO_2$ acidification from water splitting[51].

To elucidate the role of monometallic Co sites in PHE and bimetallic Fe-Co sites in $CO_2$RR, we performed DFT calculations on FeCo-NP and FeCo-NP-24. FeCo-NP is transformed to FeCo-NP-24 via nitrosyl group release with an energy penalty of 2.083 eV (Supplementary Fig. 41a amd Supplementary Table 7). Seeing Supplementary Fig. 41b–c and Supplementary Data 1, the number of electrons carried for Co and Fe metal have both decreased via light, and the charge of Co is higher than that of Fe without or with light via Bader Charge analysis, implying the catalytic active of Co may be greater relatively. Without illumination, the Co atoms have a relatively high spin density (Supplementary Fig. 41d). While under lighting, the spin density of Fe was increased (Supplementary Fig. 41e), showing the color of this FeCo-NP is influenced by the electronic transition from Co and Fe and the Fe metal is turned into one of the catalytic center to take in reaction reaction synergistically with Co via illumination. Without pre-irradiation, Fe sites in FeCo-NP are occupied by nitrosyl groups to afford monometallic Co active sites with two kinds of Co coordination environments: five-coordinate Co1 centers and four-coordinate Co2 centers with N-bound cyano groups, which are in proximity to nitrosyl groups (Supplementary Fig. 42). NO groups hindered the adsorption of $CO_2$ with Fe, which prevents Fe and Co from forming synergistic catalysis and limits the reaction of $CO_2$. The catalytic mechanism of PHE was investigated on Co1 and Co2 sites by DFT calculations. As show in Supplementary Fig. 43, $H_2O$ showed stronger adsorption on Co2 (−0.889 eV) than Co1 center (−0.830 eV). Thus, Co2 catalytic site is preferentially occupied by $H_2O$ (Co-IM0 → Co-IM1) and is the main catalytic site for PHE.

The PHE pathway on the Co2 site was investigated (Fig. 5e, Supplementary Table 8 and 10). First, the H atom dissociates from the adsorbed $H_2O$ and is bound to the Co2 site with the concomitant release of the OH (Co-IM1 → Co-IM2). At this stage, due to the saturation of the Co2 surface site, the adsorption energy of the second $H_2O$ molecule is 0.691 eV, indicating that it approaches the Co2 site via vdW forces (Co-IM2 → Co-IM3) and reacts with H through the Eley-Rideal mechanism[52]. Subsequently, the second H atom dissociates from the second $H_2O$ and is bound to the Co2 site. The two Co-bound H atoms

https://doi.org/10.1038/s41467-025-61129-x

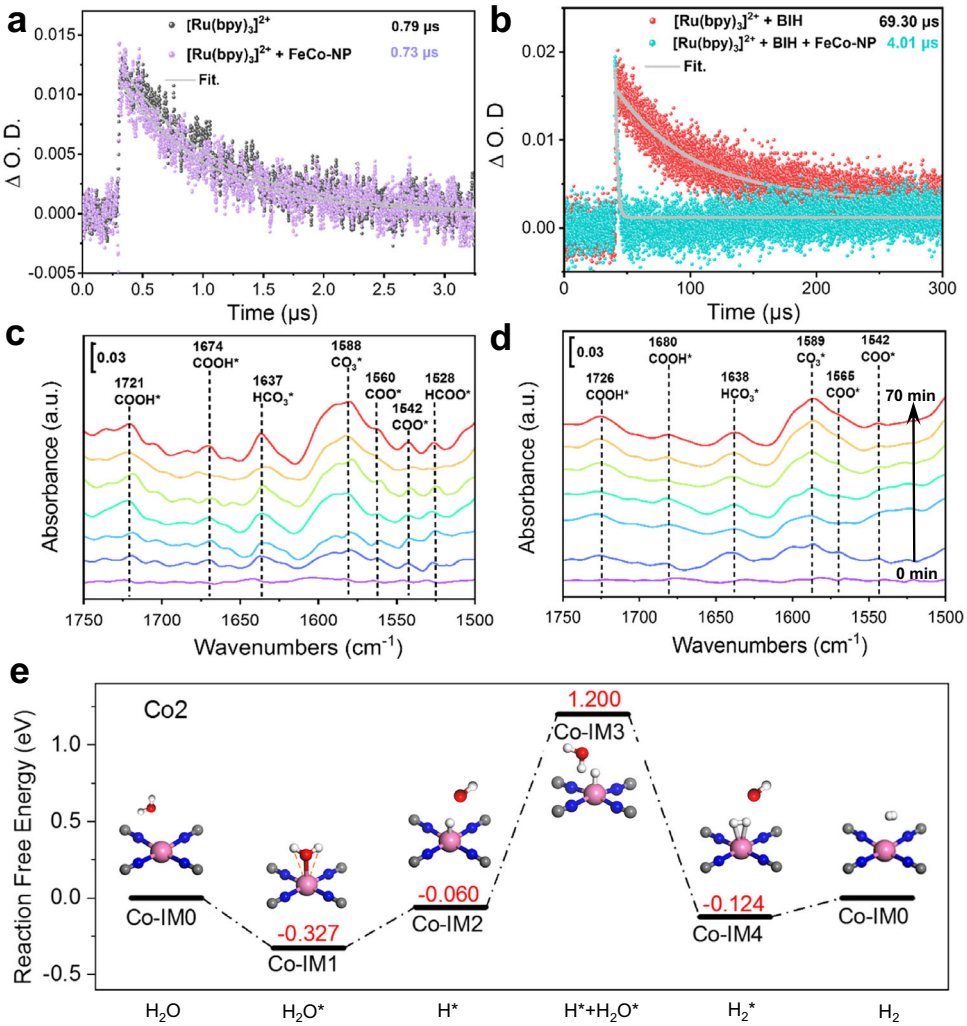


**Fig. 5 | Photocatalytic mechanism investigation. a** The decay of $[Ru(bpy)_3]^{2+}$ absorption at 455 nm with and without the addition of FeCo-NP. **b** The decay of $[Ru(bpy)_3]^{+}$ absorption at 510 nm following the addition of BIH or BIH with FeCo-NP. In situ FT-IR spectra collected during the photocatalytic $CO_2$RR and PHE over **c**, FeCo-NP-24 and **d** FeCo-NP. **e** Gibbs free energy diagram of PHE on monometallic Co sites. Source data for Fig. 5 are provided as a Source Data file.

couple into a Co-bound $H_2$ spontaneously (Co-IM3 → Co-IM4). Finally, $H_2$ dissociates from the Co2 site (Co-IM4 → Co-IM0). Since the rate-determining step (RDS) of the reaction usually involves electron-proton transfer, during the Co-IM2 to Co-IM3 stage, $H_2O$ approaches Co2 via vdW forces without involving electron-proton transfer, and thus does not constitute a RDS. Therefore, the transition from Co-IM1 to Co-IM2, with an energy barrier of 0.267 eV, is the RDS of the entire reaction.

After pre-irradiation, the exposed Fe site resulting from the nitrosyl group release enables synergistic catalysis with the adjacent Co site in FeCo-NP-24 (Supplementary Fig. 44). Both $H_2O$ and $CO_2$ reactants can adsorb on Fe and Co centers in FeCo-NP-24. $H_2O$ has larger adsorption energies of −1.125 and −1.137 eV on the Co and Fe sites, respectively, than those of $CO_2$ on the Co (−0.560 eV) and Fe (−0.565 eV) sites. Two catalytic mechanisms, namely the Fe path (Fig. 6 and Supplementary Fig. 45) and the Co path (Supplementary Figs. 46, 47), were calculated. The Fe path starts with the Fe-$H_2O$ intermediate (IM1) with $H_2O$ adsorbed on the exposed Fe site whereas the Co path begins with the Co-$H_2O$ intermediate.

After $H_2O$ adsorption on the Fe site (IM0 → IM1) along the Fe path, the OH* intermediate (IM2) forms via the dissociation of $H_2O$ on the Fe site with a free energy change of 1.291 eV (Fig. 6, Supplementary Table 9 and 11). Next, $CO_2$ was adsorbed on the Co site via TM1-OH (IM2) → TM1-OH-$CO_2$-TM2 (IM3) → TM1-O-$CO_2$-TM2 (IM5) with free energy changes of 0.331 and 0.938 eV because the Fe site is already occupied with lower free energy change (Fig. 6b and Supplementary Fig. 45). The O atom unconnected to the metal sites in IM5 undergo PCET and protonation to form and release $H_2O$ (IM5 → IM6 → IM7) with free energy changes of −1.422 and −0.154 eV. As Supplementary Fig. 48 shows, the proton-coupled electron transfer process following the *$CO_2$ intermediate determines whether HCOOH or CO is produced. Calculations reveal that protonating *$CO_2$ to *COOH and *HCOO has energy barriers of 0.16 eV and 0.89 eV, respectively. After the O-O bond in *COOH breaks to form CO and OH, only a 0.17 eV barrier remains. For *HCOO to protonate into *HCOOH, a 0.44 eV barrier must be overcome. This makes the RDS for producing HCOOH from $CO_2$ on the bimetallic active site slower. When the H atom combines with the C atom, it breaks the linear symmetry of $CO_2$, causing the transition state structure to become distorted and raising the energy barrier to 0.89 eV. Additionally, the H atom preferentially bonds with the O atom of the *$CO_2$ intermediate (due to the lone pair electrons on O being more prone to combine with H, with the energy barrier for the IM7 → IM8 process being only 0.16 eV). As a result, most reactants follow the pathway to generate CO (IM7 → IM8 → IM9), reducing the effective reaction ratio for producing HCOOH. Consequently, this lowers the yield of HCOOH and increases the selectivity for CO production. In

https://doi.org/10.1038/s41467-025-61129-x

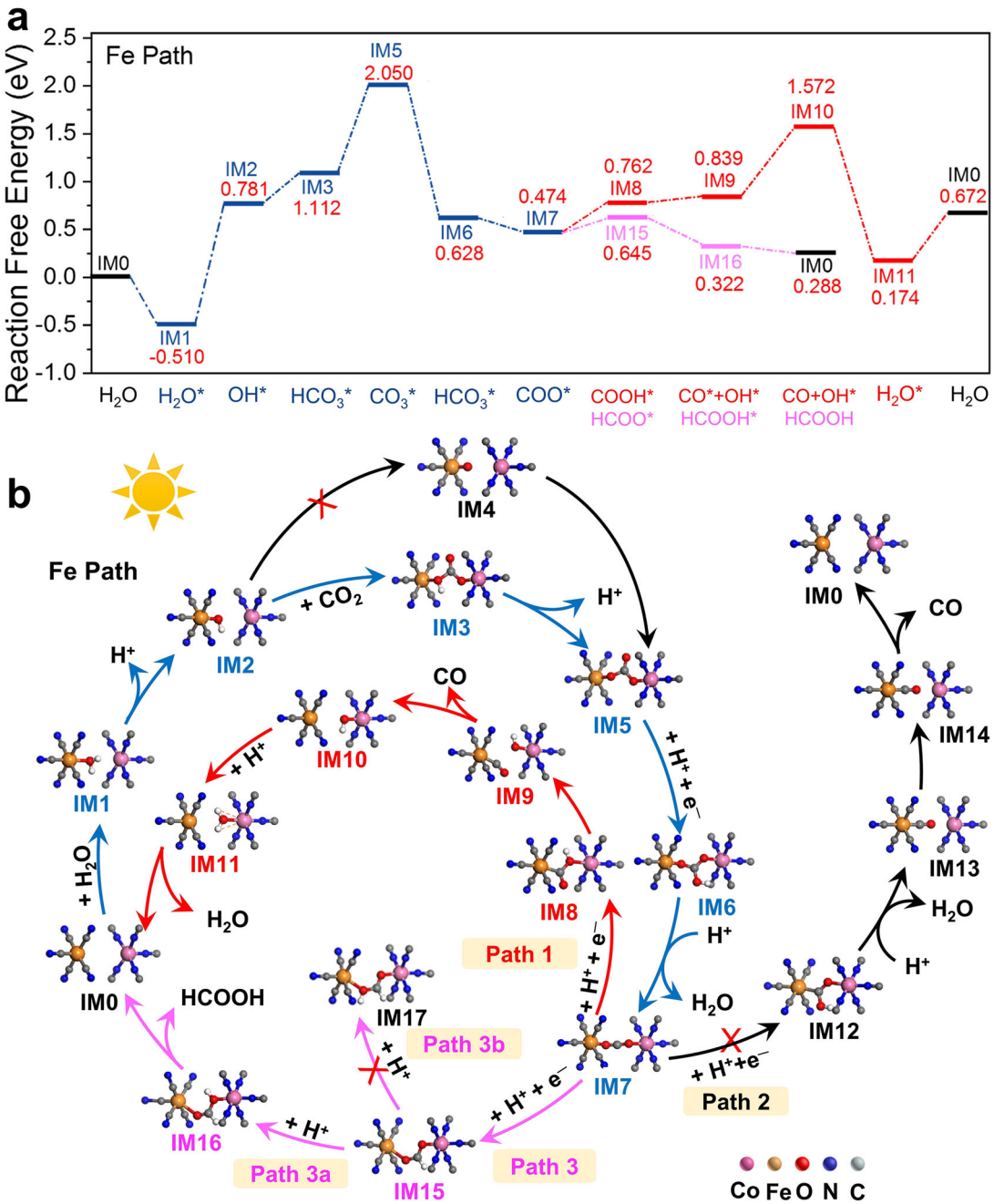


**Fig. 6 | Bimetallic catalytic mechanism in FeCo-NP-24. a** The Gibbs free energy diagram for CO and HCOOH production on bimetallic Fe-Co sites. The red values stand for the reaction-free energies. **b** The reaction intermediate structures for CO and HCOOH production via the Fe path on bimetallic Fe-Co sites. Source data for Fig. 6 are provided as a Source Data file.

summary, this is consistent with the experimental results shown in Fig. 4b, c. The Co path was also calculated to show the largest free energy change of 1.398 eV in the reaction pathway (Supplementary Figs. 46, 47). In the PHE reaction mechanism of FeCo-NP-24, the dissociation process requires overcoming a free energy barrier of 2.899 eV (Supplementary Figs. 49). Thus, the optimal path for the formation of IM7 from IM0 is through the Fe path as shown in Fig. 6a with the largest free energy charge of 1.291 eV.

The binding form of TM1-$CO_2$-TM1 intermediate affects the selectivity of $CO_2$ reduction in the diatomic sites[47]. The intermediate IM7 can be hydrogenated via three paths: (1) PCET to the Co-bonded O to form Fe-CO-OH-Co species (IM8), (2) PCET to Fe-bonded O with the formation of the Fe-C bond (IM12), (3) PCET to the C atom (IM15) (Fig. 6b). Dual-atom synergistic catalysis boosts the cleavage of C-O bond between TM1-C-O-TM2 to produce CO[53,54]. The largest free energy changes of Path 1 and 2 are 0.733 and 1.395 eV, respectively (Fig. 6b and Supplementary Fig. 45). Compared with Path 1 and Path 2, the Path 1 favors reducing the activation energy in the RDS during the $CO_2$-to-CO photoreduction process. Thus, CO is preferentially produced via the Fe-COOH-Co species (Path 1) in the Fe path with the adsorbed $H_2O$ dissociation as the RDS (IM1 → IM2 with a free energy change of 1.291 eV). The Fe-OCO-Co species allows rapid protonation at the C atom to form Fe-OCHO-Co intermediate (IM15) by the synergistic effect of bimetallic Fe-Co sites[18,55,56]. In Path 3, the Fe-OCHO-Co intermediate (IM15) forms with free energy change of 0.171 eV. IM15 can be protonated at the Co-bonded O via IM15 → IM16 → IM0 (Path 3a with free energy changes of −0.323 and −0.034 eV) or at the Fe-bonded O via IM15 → IM17 → IM0 (Path 3b with free energy changes of −0.515

and 0.315 eV). Thus, the HCOOH is preferentially produced via Path 3a with lower free energy changes. In the Co path, the hydrogenation paths were similar to those of the Fe path, but energy changes along the Co path are higher than those of the Fe path (Supplementary Figs. 46, 47). Thus, DFT calculations support selective $H_2$ evolution by monometallic Co sites in FeCo-NP and photocatalytic reduction of $CO_2$ to CO and HCOOH by bimetallic Fe-Co sites in FeCo-NP-24.

## Discussion

In this work, we have tranformed monometallic Co sites in FeCo-NP to bimetallic Fe-Co sites in FeCo-NP-24 via photo-induced release of nitrosyl groups to tune the photocatalytic activity from PHE to $CO_2$RR. FeCo-NP efficiently catalyzes PHE with 28.5 mmol $g^{-1}$ yield and 85.4% selectivity for $H_2$. On the other hand, the bimetallic Fe-Co sites in FeCo-NP-24 efficiently catalyze $CO_2$ photoreduction to produce C1 products with 31.5 mmol $g^{-1}$ yield and 87.3% selectivity. Systematic investigations revealed that the PHE activity of monometallic Co sites results from adsorption affinity for $H_2O$ and subsequential O-H bond cleavage steps. The bimetallic Fe-Co sites in FeCo-NP-24 strongly adsorb both $H_2O$ and $CO_2$ and hydrogenate O and C centers in key steps to produce CO and HCOOH, respectively. We demonstrated the facile transformation of monometallic Co sites to bimetallic Fe-Co sites via light irradiation, which provides an efficient strategy to control the competing reactions of PHE and $CO_2$RR by regulating catalytically active sites at a molecular level. The expansion of the reaction scope of synergistic bimetallic catalysts to $N_2$ reduction and other important reactions promises to enable their widespread applications in enviroenmental remediation and clean energy production.

## Methods

### Materials

All of the chemicals were obtained from commercial sources and used without further purification. Sodium nitroferricyanide dehydrate (99.0%, $Na_2[Fe(CN)_5NO]{\cdot}2H_2O$, HEOWNS), Zinc acetate (99.0%, $Zn(OAc)_2{\cdot}2H_2O$, General-Reagent), cobalt acetate (99.5%, $Co(OAc)_2{\cdot}4H_2O$, Macklin), tris(2,2′-bipyridyl)rutheniumchloride hexahydrate (99.9 %, $[Ru(bpy)_3Cl_2]{\cdot}6H_2O$, HEOWNS), imidazole (99.0 %, Adamas), sodium sulfate (98.0 %, $Na_2SO_4$, Adamas). 1,3-dimethyl-2-phenyl-2,3-dihydro-1Hbenzo[d]imidazole (97%, BIH, Energy Chemical). Nafion solution (5.0 wt%, Sigma-aldrich), tetrabutylammonium hexafluorophosphate (99.0 %, $Bu_4NPF_6$, Adamas), methanol (99.5% MeOH, Fuchen), ethanol (99.7% EtOH, Fuchen), acetonitrile (99.5 %, $CH_3CN$, Fuchen), and deionized water, deuterium oxide ($D_2O$, Innochem) were used without further purification.

### Synthesis of FeCo-NP

FeCo-NP was synthesized according to the reported method with modifications[30,57,58]. First, sodium nitroferricyanide dihydrate (30 mg, 0.1 mmol) was dissolved in a mixed solution of deionized water (8 mL) and methanol (2 mL). Then, cobalt acetate tetrahydrate (25 mg, 0.1 mmol) was dissolved in 10 mL mixed solution of deionized water (8 mL) and methanol (2 mL). The $Co(OAc)_2$ solution was added dropwise to the sodium nitroferricyanide solution within 5 min under stirring at room temperature (25 °C). The pink solid particles gradually formed in the mixed solution. After stirring for 3 h and aging at room temperature (25 °C) for 24 h, the resulting pink precipitate was collected by centrifugation and washed three times with deionized water and methanol, respectively. Finally, the resultant FeCo-NP was dried at 60 °C under vacuum overnight.

### Large-scale preparation

The synthesis of FeCo-NP was scaled-up via proportionally increasing the starting materials. For instance, 100 g sodium nitroferricyanide dehydrate (0.35 mol) and 88 g cobalt acetate tetrahydrate (0.35 mol) were mixed in 6 L mixed solvents to synthesize 102.8 g FeCo-NP.

### Synthesis of FeCo-NP-n

FeCo-NP-n was synthesized by photoinduced conversion of FeCo-NP. The as-synthesized FeCo-NP (25 mg) was dispersed in 25 mL of deionized water and then placed in a Pyrex tube, which was sealed with a rubber septum and deaerated with argon for 20 min. Then, FeCo-NP was irradiated with a 300 W Xe lamp (200 mW $cm^{-2}$) for different times (2, 6, 12, and 24 h) to obtain the samples of FeCo-NP-2, FeCo-NP-6, FeCo-NP-12, and FeCo-NP-24, respectively. The samples were collected by centrifugation and washed three times with deionized water and methanol, respectively. Finally, the FeCo-NP-n was dried at 60 °C under vacuum overnight.

According to previous studies[59], the NO group in $[Fe(CN)_5NO]^{2-}$ was released via the photon absorption pathway. The detailed photolysis mechanism is listed as follows:

$$[Fe^{2+}(CN)_5NO^+]^{2-} \xrightarrow{h\nu} [Fe(CN)_5]^{3-} + NO^+ \quad (1)$$

$$NO^+ + H_2O \rightarrow 2H^+ + NO_2{}^+ \quad (2)$$

$$[Fe(CN)_5]^{3-} + H_2O \rightarrow [Fe(CN)_5H_2O]^{3-} \quad (3)$$

$$[Fe(CN)_5H_2O]^{3-} + H^+ \rightarrow [Fe(CN)_5H_3O]^{2-} \quad (4)$$

Reaction (2) explains the decrease of pH after irradiation.

### Synthesis of FeZn-NP

The preparation of FeZn-NP was similar to FeCo-NP, except that $Co(OAc)_2$ is replaced by $Zn(OAc)_2$.

### Synthesis of Co[Fe(CN)$_5$Im]

According to the reported method[60], sodium nitroferricyanide dihydrate (26 mg, 0.1 mmol) was dissolved in a mixed solution of 16 mL water and 4 mL ethanol followed by the addition of 1 mmol imidazole. After stirring at 60 °C for 12 h, the yellow crystals were collected by filtration and dissolved in a mixed solution of 8 mL deionized water and 2 mL methanol. Then, cobalt acetate tetrahydrate (25 mg, 0.1 mmol) in a mixed solution of water and methanol ($H_2O$: $CH_3OH$ = 4: 1, 10 mL) was dropwise added to the above solution. After stirring for 3 h and aging at room temperature (25 °C) for 24 h, the resulting pink precipitate was collected by centrifugation and washed several times with deionized water.

### Catalyst characterization

Powder X-ray diffraction (PXRD) was performed on a Rigaku X-Ray Diffractometer (D/teX Ultra 250). X-ray photoelectron spectroscopy (XPS) was conducted on a PHI ESCA-5000C photoelectron spectrometer. The morphologies of the samples were studied on a field-emission scanning electron microscope (SEM, Hitachi, S-4800). Transmission electron microscope (TEM) and high-resolution TEM (HRTEM, JEOL-2100F) investigations were carried out on the microscope with an accelerate voltage of 200 kV. Light absorption was characterized by ultraviolet-visible (UV-Vis) spectroscopy (Lambda 750 UV/VIS/NIR). Fourier transform-infrared (FT-IR) spectroscopy was performed on Frontier Mid-IR FTIR/STA6000-TL9000-Clarus SQ8 (Perkin Elmer). In situ Raman spectroscopy was performed on a Raman spectroscopy (HORIBA Evolution, HORIBA JOBIN YVON S.A.S.) equipped with a 532 nm laser. For potential-resolved operando Raman spectroscopy, the collection time was 10 min. The photoluminescence (PL) spectra were collected on a fluorescence spectrophotometer (F-7000, Hitachi, Japan). Transient absorption spectra were measured on the LP980 laser flash photolysis instrument (Edinburgh, UK). Elemental analysis were measured on the Vario EL Cube (Elementar, Germany). Thermogravimetric (TG) analyses were performed on a

NETZSCH TG 209 thermogravimetric analyzer in an Ar atmosphere with a heating rate of 10 °C $min^{-1}$. The in-situ Fourier transform infrared spectra were tested using a Frontier Mid-IR FTIR/CRCP-7070-A (BRUKER TENSOR 27) with KBr as the diluent. For FT-IR experiments, the infrared beam path inside the accessory and the rest of the sample compartment were held under an Ar flow to avoid atmospheric water and $CO_2$ absorption. Before the start of photocatalysis, the system was flowed with Ar for 20 min followed by $CO_2$ for 15 min to remove oxygen and solvent molecules. Then the reaction chamber was sealed under 1 atm $CO_2$.

### TGA–FTIR experiment

The thermogravimetric analyzer (NETZSCH, 209F3A) was coupled to the FTIR spectrophotometer (STA449F5 Jupiter Nicolet iS50) to investigate the mass loss and formation of catalysts at the same time. In the TGA experiment, the sample was heated from 40 to 900 °C at heating rate of 10 °C/min under the inert atmosphere. During the experiment the cell of TGA is flushed with nitrogen to maintain an inert atmosphere for thermal decomposition of the sample. The FTIR is connected to TGA by a flow cell which is heated to 200 °C to prevent condensation of the produced gases on the cell wall. The FTIR spectrometer is set to collect 32 interferograms at a resolution of 4 wavenumbers with a scanning rate of 0.6329 cm/s and the spectral range is set to be 4000–400 $cm^{-1}$. All the interferograms are collected during the pyrolysis and post-processed to obtain the absorption spectra and the corresponding gas formation profiles.

### XAS analysis

XANS spectra at the Fe K-edge in transmission mode were collected at Beamline 10-BM-A at the Advanced Photon Source (APS) at Argonne National Laboratory. The hard X-ray was monochromatized with Si(111) double crystals and detuned by 50% to reduce the contribution of higher-order harmonics below the level of noise. A metallic Fe foil standard was used as a reference for energy calibration and was measured simultaneously with experimental samples. The incident beam intensity ($I_0$), transmitted gas compositions of 94% $N_2$ and 6% He, 57% $N_2$ and 43% Ar, and 100% $N_2$, respectively. Multiple X-ray absorption spectra were collected at room temperature (25 °C) for each sample. Samples were ground and mixed with polyethyleneglycol (PEG) and packed in a 6-shooter sample holder to achieve adequate absorption length.

The acquired EXAFS data were extracted and processed according to the standard procedures using the Athena module implemented in the IFEFFIT software package. Before merging, spectra were calibrated against the reference spectra and aligned to the first peak in the smoothed first derivative of the absorption spectrum. The spectra were deglitched to remove the background noises and processed to obtain a normalized unit edge step. Fitting of the EXAFS region was performed using the Artemis program of the IFEFFIT package. Subsequently, $k^3$-weighted $\chi$(k) data in the k-space were Fourier transformed to real R space using a hanging window to separate the EXAFS contributions from different coordination shells. $k^3$-weighted wavelet transformed (WT) EXAFS analysis, featured simultaneous resolution in both k and R spaces. A k-range of 0–12 $Å^{-1}$ and R-range of 0–4 Å were as used to generate the magnitude of the Fourier transform. Refinement was performed by optimizing an amplitude factor $S_0^2$ and energy shift $\Delta E_0$ which are common to all paths, in addition to parameters for bond length ($\Delta R$) and Debye-Waller factor ($\sigma^2$). The fitting model for Fe was based on the single crystal structure from CCDC 1730889.

### Photocatalysis

Photocatalytic experiments with 1 mg catalysts were performed in a 5 mL $CO_2$-saturated $H_2O/CH_3CN$ solution (v: v = 1: 9) under ambient conditions with 1 mg $[Ru(bpy)_3]Cl_2$ and 14 mg of BIH. Ar and $CO_2$ were sequentially bubbled into the reactor for 15 min. During the photocatalytic process, the reaction system was vigorously stirred at room temperature under irradiation of a 300 W Xe lamp (25 °C, 100 mW $cm^{-2}$) without AM 1.5 G filter. The generated gas products were analyzed by a GC-2014 gas chromatograph instrument (SHIMADZU) equipped with TCD and FID dual detectors. The liquid phase of the reaction system was analyzed by an ion chromatograph (IC, DX-600, Dionex).

### Photocatalysis control experiments

Control experiments with 1 mg catalyst were performed in a 5 mL $H_2O/CH_3CN$ solution under ambient conditions with 1 mg $[Ru(bpy)_3]Cl_2$ and 14 mg of BIH. The experiments in entries 2 and 3 were conducted without PSs or in the dark, and the experiments in entries 4-6 by increasing the $H_2O$ to $CH_3CN$ ratio from 1: 24 to 1: 4 with FeCo-NP. The experiments in entries 7 and 8 with FeCo-NP were performed in a 5 mL $CO_2$ or Ar saturated $H_2O/CH_3CN$ solution (v: v = 1: 9), respectively, and the experiment in entry 9 was performed in a Ar saturated solution with FeCo-NP-24. The catalyst mass-dependent experiments were performed by proportionally increasing the reagents, including $H_2O/CH_3CN$ solution, $[Ru(bpy)_3]Cl_2$, and BIH. During the photocatalytic process, the reaction system was vigorously stirred at room temperature under irradiation of a 300 W Xe lamp (25 °C, 100 mW $cm^{-2}$).

### Recycle test

In the photocatalytic system, the stability of FeCo-NP-24 was evaluated by repeat photocatalytic experiments with the recycled catalyst at 4 h intervals. After every cycle, FeCo-NP-24 was collected by centrifugation, dried, and then used for the next cycle of the experiment. The generated gases were analyzed by GC, while the generated liquid phase was evaluated by ion chromatography. After recycling experiments, the catalyst was collected by centrifugation and washed several times with deionized water and methanol, and then dried at 60 °C in vacuum overnight. Then, the integrity of the recovered FeCo-NP-24 after the photocatalytic experiments was confirmed by PXRD.

### Photoelectrochemical test

To conduct photoelectrochemical and electrochemical studies, different samples were first prepared by mixing 5 mg photocatalysts with 20 μL of Nafion and 180 μL of ethanol to make a uniform slurry under ultrasonication. Then, 20 μL of the slurry was dropped onto fluorine-doped tin oxide (FTO) glass electrodes (1 $cm^2$) as working electrodes. Electrochemical measurements were carried out in a conventional three-electrode cell using a CHI760E electrochemical workstation. A platinum plate and an Ag/AgCl electrode (GaossUnion) were used as the counter and reference electrodes, respectively. Electrochemical impedance spectroscopy (EIS) measurements were carried out at the open circuit potential over the frequency range of $10^{-2}$–$10^5$ Hz. Mott-Schottky plots were acquired at frequencies of 0.5, 1.0, and 2 kHz. Transient photocurrent measurements were performed at 0.4 V with an illumination/dark interval of 10 s. These measurements were carried out in a 0.05 M $Na_2SO_4$ solution. All electrochemical experiments were conducted under ambient temperature conditions (25 °C).

### Cyclic voltammetry

The CV curves were measured in a degassed $CH_3CN/H_2O$ (v/v, 9/1) solution, containing 0.5 mM $[Ru(bpy)_3]Cl_2$, ferrocene, and 0.10 M $Bu_4NPF_6$ as the supporting electrolyte. The scan rate was 0.1 $V/s^{-1}$ with a positive initial scanning direction. Glassy carbon electrode, Pt silk, and $Ag/AgNO_3$ (GaossUnion) were used as the working electrode, counter electrode, and reference electrode, respectively. All electrochemical experiments were conducted under ambient temperature conditions (25 °C).

### Transient absorption spectra

Transient absorption spectra of $[Ru(bpy)_3]^{2+}$ and catalysts were measured on the LP980 laser flash photolysis instrument (Edinburgh, UK) with a light source of 150 W Xe lamp. Before each measurement, the $[Ru(bpy)_3]^{2+}$ (0.05 mM) solution was bubbled with Ar for 15 min. Upon pulsed laser excitation at 450 nm, the excited state lifetime of $[Ru(bpy)_3]^{2+}$, $[Ru(bpy)_3]^{2+}$/catalyst (5 mM catalyst), or $[Ru(bpy)_3]^{2+}$/BIH (50 mM BIH) was measured at 455 nm. The excited state lifetime of $[Ru(bpy)_3]^{2+}$ with 50 mM BIH and $[Ru(bpy)_3]^{2+}$ in the presence of both BIH (50 mM) and catalysts (5 mM) were measured at 510 nm.

### Isotope tracing experiments

Isotope tracing experiments were performed in a 5 mL $^{13}CO_2$-saturated $H_2O/CH_3CN$ (v: v = 1: 9) solution and $CO_2$-saturated $D_2O/CH_3CN$ (v: v = 1: 9) solution under ambient conditions with 1 mg $[Ru(bpy)_3]^{2+}$ as the PS and 14 mg BIH as the scarified reagent. The solvent was deaerated with argon for 30 min. Then, high-purity $^{13}CO_2$ was introduced into the reactor with a partial pressure of 1.0 atm. A 300 W Xe lamp was used as the light source. $D_2$ and $^{13}CO$ were analyzed by a mass spectrometer (Hiden HPR20) and gas chromatograph-mass spectrometer (GC-MS, Agilent 7890B/5977B), respectively. $^{13}C$ NMR spectra were tested on a $^{13}C$ NMR instrument (Bruker AVANCE III HD NMR 400 MHz) with total proton decoupling.

### Computational details

All spin-polarized density function theory (DFT) calculations were performed in the Vienna Ab initio Simulation Program (VASP)[61]. The Projector Augmented Wave (PAW) method was employed to describe the interactions between ions and electrons[62]. The Perdew-Burke-Ernzerhof (PBE) functional within the framework of generalized gradient approximation (GGA) was utilized for the exchange-correlation energy of interacting electrons[63,64]. The convergence thresholds and energy change in self-consistent field (SCF) were set to a maximum force less than 0.02 eV $Å^{-1}$ and $1 \times 10^{-6}$ eV on each atom, respectively. The DFT-D3 method was incorporated to account for dispersion interactions of van der Waals (vdW) by Grimme´s scheme means[65]. The adsorption energy of intermediates on FeCo-NP was computed as following:

$$E_{ads} = E_{tot} - E_{substrate} - E_{adsorbate} \quad (5)$$

where $E_{tot}$, $E_{substrate}$, and $E_{adsorbate}$ are the total energies of the FeCo-NP with adsorbate, FeCo-NP, and isolated adsorbed pieces in vacuum, respectively. The computational hydrogen electrode (CHE) model, proposed by Nørskov et al.[66], was adopted to evaluate the free energy ($\Delta G$) for elementary steps in all reaction processes. And the standard hydrogen electrode (SHE) model (i.e., $H^+ + e^- \leftrightarrow 1/2H_2$) was also used[67]. The reaction free energy is defined as:

$$\Delta G = \Delta E + \Delta ZPE - T\Delta S - neU + (pH)k_B T \ln 10 \quad (6)$$

where $\Delta E$ stands for the change of energy obtained from the DFT calculations, $ZPE$ is the zero-point energy, $T$ is the temperature, and $\Delta S$ is the entropy change. n is the number of electrons transferred in the reaction, $e$ is the transferred charge, and the $U$ is the potential applied at the electrode. $k_B$ is the Boltzmann constant, the value of $pH$ is set to be 0, and $T$ is set to 298.15 K.

All optimized atomic configurations as CONTCAR-formatted structure files and energy profiles of reaction intermediates, generated via DFT calculations, have been archived in Supplementary Tables 7–10 and Supplementary Data 1.

## Data availability

The data that support the findings of this study are available within the paper and Supplementary Information files or available from the corresponding author. Source data are provided with this paper.

## References


1. Rekker, S. et al. Evaluating fossil fuel companies' alignment with 1.5 °C climate pathways. *Nat. Clim. Chang.* **13**, 927–934 (2023).
2. Rahimpour, S. et al. Selected social impact indicators influenced by materials for green energy technologies. *Nat. Commun.* **15**, 9336 (2024).
3. Lv, J. et al. Solar utilization beyond photosynthesis. *Nat. Rev. Chem.* **7**, 91–105 (2023).
4. Nishiyama, H. et al. Photocatalytic solar hydrogen production from water on a 100-$m^2$ scale. *Nature* **598**, 304–307 (2021).
5. Bonchio, M. et al. Best practices for experiments and reporting in photocatalytic $CO_2$ reduction. *Nat. Catal.* **6**, 657–665 (2023).
6. Nishioka, S. et al. Photocatalytic water splitting. *Nat. Rev. Methods Prim.* **3**, 42 (2023).
7. Liu, Y. et al. Improving $CO_2$ photoconversion with ionic liquid and Co single atoms. *Nat. Commun.* **14**, 1457 (2023).
8. Yin, H.-Q., Zhang, Z.-M. & Lu, T.-B. Ordered integration and heterogenization of catalysts and photosensitizers in metal-/covalent-organic frameworks for boosting $CO_2$ photoreduction. *Acc. Chem. Res.* **56**, 2676–2687 (2023).
9. Xie, Y. et al. High carbon utilization in $CO_2$ reduction to multi-carbon products in acidic media. *Nat. Catal.* **5**, 564–570 (2022).
10. Jiao, L., Wang, J. & Jiang, H.-L. Microenvironment modulation in metal–organic framework-based catalysis. *Acc. Mater. Res.* **2**, 327–339 (2021).
11. Fang, S. et al. Photocatalytic $CO_2$ reduction. *Nat. Rev. Methods Prim.* **3**, 61 (2023).
12. Jiang, Z. et al. Filling metal-organic framework mesopores with $TiO_2$ for $CO_2$ photoreduction. *Nature* **586**, 549–554 (2020).
13. Guo, S. et al. Switching excited state distribution of metal-organic framework for dramatically boosting photocatalysis. *Angew. Chem. Int. Ed.* **61**, e202206193 (2022).
14. Fu, P. et al. Covalent organic framework stabilized Single $CoN_4Cl_2$ site boosts photocatalytic $CO_2$ reduction into tunable syngas. *Angew. Chem. Int. Ed.*, https://doi.org/10.1002/anie.202415202 (2024).
15. Zhuo, T. C. et al. H-bond-mediated selectivity control of formate versus CO during $CO_2$ photoreduction with two cooperative Cu/X sites. *J. Am. Chem. Soc.* **143**, 6114–6122 (2021).
16. Ouyang, T. et al. A dinuclear cobalt cryptate as a homogeneous photocatalyst for highly selective and efficient visible-light driven $CO_2$ reduction to CO in $CH_3CN/H_2O$ solution. *Angew. Chem. Int. Ed.* **56**, 738–743 (2017).
17. Ouyang, T. et al. Dinuclear metal synergistic catalysis boosts photochemical $CO_2$ -to-CO conversion. *Angew. Chem. Int. Ed.* **57**, 16480–16485 (2018).
18. Guo, Z. et al. Selectivity control of CO versus $HCOO^-$ production in the visible-light-driven catalytic reduction of $CO_2$ with two cooperative metal sites. *Nat. Catal.* **2**, 801–808 (2019).
19. Nishioka, S. et al. Surface-modified, dye-sensitized niobate nanosheets enabling an efficient solar-driven Z-scheme for overall water splitting. *Sci. Adv.* **8**, eadc9115 (2022).
20. Liu, L. et al. Water-stable nickel metal-organic framework nanobelts for cocatalyst-free photocatalytic water splitting to produce hydrogen. *J. Am. Chem. Soc.* **144**, 2747–2754 (2022).
21. Yan, X. et al. An electron-hole rich dual-site nickel catalyst for efficient photocatalytic overall water splitting. *Nat. Commun.* **14**, 1741 (2023).
22. Xue, Z.-H. et al. Single-atom catalysts for photocatalytic energy conversion. *Joule* **6**, 92–133 (2022).

23. Pu, T. et al. Dual atom catalysts for energy and environmental applications. *Angew. Chem. Int. Ed.* **62**, e202305964 (2023).
24. Hai, X. et al. Scalable two-step annealing method for preparing ultra-high-density single-atom catalyst libraries. *Nat. Nanotechnol.* **17**, 174–181 (2022).
25. Yang, Y. et al. O-coordinated W-Mo dual-atom catalyst for pH-universal electrocatalytic hydrogen evolution. *Sci. Adv.* **6**, eaba6586 (2020).
26. Li, J. et al. Self-adaptive dual-metal-site pairs in metal-organic frameworks for selective $CO_2$ photoreduction to $CH_4$. *Nat. Catal.* **4**, 719–729 (2021).
27. Nam, D. H. et al. Molecular enhancement of heterogeneous $CO_2$ reduction. *Nat. Mater.* **19**, 266–276 (2020).
28. Iemhoff, A., Vennewald, M. & Palkovits, R. Single-atom catalysts on covalent triazine frameworks: at the crossroad between homogenous and heterogeneous catalysis. *Angew. Chem. Int. Ed.* **62**, e202212015 (2023).
29. Cammarata, M. et al. Charge transfer driven by ultrafast spin transition in a CoFe Prussian blue analogue. *Nat. Chem.* **13**, 10–14 (2021).
30. Ohkoshi, S. I. et al. A photoswitchable polar crystal that exhibits superionic conduction. *Nat. Chem.* **12**, 338–344 (2020).
31. Wang, A. et al. Enhanced and synergistic catalytic activation by photoexcitation driven S–scheme heterojunction hydrogel interface electric field. *Nat. Commun.* **14**, 6733 (2023).
32. Sun, K. et al. $Co(CN)_3$ catalysts with well-defined coordination structure for the oxygen reduction reaction. *Nat. Catal.* **6**, 1164–1173 (2023).
33. Yu, X. et al. Highly luminescent lanthanide metal-organic frameworks with tunable color for nanomolar detection of iron(III), ofloxacin and gossypol and anti-counterfeiting applications. *Angew. Chem. Int. Ed.* **62**, e202306680 (2023).
34. Rodríguez-Hernández, J. et al. Silver nitroprusside: Atypical coordination within the metal nitroprussides series. *Inorg. Chim. Acta* **428**, 51–56 (2015).
35. Hidenari, I. et al. Thermal decomposition of prussian blue analogues of the type $Fe[Fe(CN)_5NO]$. *Z. Naturforsch. B* **55**, 685–690 (2000).
36. Shimokawabe, M. et al. Temperature programmed desorption and infrared spectroscopic studies of nitrogen monoxide adsorbed on ion-exchanged copper mordenite catalysts. *Appl. Catal. A-Gen.* **166**, 215–223 (1998).
37. Reguera, L., Avila, Y. & Reguera, E. Transition metal nitroprussides: Crystal and electronic structure, and related properties. *Coord. Chem. Rev.* **434**, 213764 (2021).
38. Lynch, M. S. et al. Probing the photoinduced metal-nitrosyl linkage isomerism of sodium nitroprusside in solution using transient infrared spectroscopy. *J. Am. Chem. Soc.* **133**, 5255–5262 (2011).
39. Liang, X. et al. High proton conductivity modulated by active protons in 1D ultra-stable metal–organic coordination polymers: a new insight into the coordination interaction/ability of metal ions. *Inorg. Chem. Front.* **10**, 1238–1254 (2023).
40. Stochel, G. et al. Kinetics and mechanism of the acid-catalyzed aquation and base hydrolysis of nitropentacyanoferrate(III) in aqueous solution. Evidence for a pseudo-zero-order hydrolysis process. *Inorg. Chem.* **27**, 2767–2770 (1988).
41. Pressprich, M. R. et al. Analysis of a metastable electronic excited state of sodium nitroprusside by X-ray crystallography. *J. Am. Chem. Soc.* **116**, 5233–5238 (1994).
42. Tchana Kamgne, D. et al. An experimental XAS and ab initio approach to describe the electronic and local structure of sodium nitroprussiate single crystals. *J. Mol. Struct.* **1245** (2021).
43. Xue, G., Dai, Q. & Jiang, S. Chemical reactions of imidazole with metallic silver studied by the use of SERS and XPS techniques. *J. Am. Chem. Soc.* **110**, 2393–2395 (1988).
44. Zhao, Y. et al. Industrial-current-density $CO_2$-to-$C_{2+}$ electroreduction by anti-swelling anion-exchange ionomer-modified oxide-derived Cu nanosheets. *J. Am. Chem. Soc.* **144**, 10446–10454 (2022).
45. Wang, H. et al. Efficient solar-driven $CO_2$ methanation and hydrogen storage over nickel catalyst derived from metal-organic frameworks with rich oxygen vacancies. *Adv. Sci.* **10**, 2304406 (2023).
46. Mondal, B. et al. Intermediates involved in the $2e^-/2H^+$ reduction of $CO_2$ to CO by iron(0) porphyrin. *J. Am. Chem. Soc.* **137**, 11214–11217 (2015).
47. Li, Y. et al. Promoting $CO_2$ methanation via ligand-stabilized metal oxide clusters as hydrogen-donating motifs. *Nat. Commun.* **11**, 6190 (2020).
48. Matsubu, J. C. et al. Adsorbate-mediated strong metal-support interactions in oxide-supported Rh catalysts. *Nat. Chem.* **9**, 120–127 (2017).
49. Amanullah, S., Saha, P. & Dey, A. Activating the Fe(I) state of iron porphyrinoid with second-sphere proton transfer residues for selective reduction of $CO_2$ to HCOOH via Fe(III/II)-COOH intermediate(s). *J. Am. Chem. Soc.* **143**, 13579–13592 (2021).
50. Zhu, S. et al. Direct observation on reaction intermediates and the role of bicarbonate anions in $CO_2$ electrochemical reduction reaction on Cu surfaces. *J. Am. Chem. Soc.* **139**, 15664–15667 (2017).
51. Chernyshova, I. V., Somasundaran, P. & Ponnurangam, S. On the origin of the elusive first intermediate of $CO_2$ electroreduction. *PNAS* **115**, E9261–E9270 (2018).
52. Prins, R. Eley–Rideal, the Other Mechanism. *Top. Catal.* **61**, 714–721 (2018).
53. Gong, Y. N. et al. A planar-structured dinuclear cobalt(II) complex with indirect synergy for photocatalytic $CO_2$-to-CO conversion. *Angew. Chem. Int. Ed.*, e202411639 (2024).
54. Bharti, J. et al. Visible-light-driven $CO_2$ reduction with homo-bimetallic complexes. cooperativity between metals and activation of different pathways. *J. Am. Chem. Soc.* **145**, 25195–25202 (2023).
55. Deng, S. et al. Dual lewis acid-base sites regulate silver-copper bimetallic oxide nanowires for highly selective photoreduction of carbon dioxide to methane. *Angew. Chem. Int. Ed.* **62**, e202309625 (2023).
56. Jiang, Z. et al. A bismuth-based zeolitic organic framework with coordination-linked metal cages for efficient electrocatalytic $CO_2$ reduction to HCOOH. *Angew. Chem. Int. Ed.* **62**, e202311223 (2023).
57. Zhong, L. et al. Construction of hierarchical photocatalysts by growing $ZnIn_2S_4$ nanosheets on Prussian blue analogue-derived bimetallic sulfides for solar co-production of $H_2$ and organic chemicals. *J. Energy Chem.* **54**, 386–394 (2021).
58. Singh, B. et al. Deciphering ligand controlled structural evolution of prussian blue analogues and their electrochemical activation during alkaline water oxidation. *Angew. Chem. Int. Ed.* **61**, e202211585 (2022).
59. Mitra, R. P. et al. Photolysis of sodium nitroprusside and nitroprussic acid. *J. Inorg. Nucl. Chem.* **25**, 1263–1266 (1963).
60. Toma, H. E., Martins, J. M. & Giesbrecht, E. Kinetics of reaction of imidazole, glycine, and L-histidine with the aqua-pentacyanoferrate (II) ion. *J. Chem. Soc. Dalton Trans.* **12**, 1610–1617 (1978).
61. Kresse, G. & Furthmuller, J. Efficient iterative schemes for ab initio total-energy calculations using a plane-wave basis set. *Phys. Rev. B* **54**, 11169–11186 (1996).
62. Kresse, G. & Joubert, D. From ultrasoft pseudopotentials to the projector augmented-wave method. *Phys. Rev. B* **59**, 1758–1775 (1999).
63. Ernzerhof, M. & Perdew, J. P. Generalized gradient approximation to the angle- and system-averaged exchange hole. *J. Chem. Phys.* **109**, 3313–3320 (1998).

64. Perdew, J. P., Burke, K. & Ernzerhof, M. Generalized gradient approximation made simple. *Phys. Rev. Lett.* **77**, 3865–3868 (1996).
65. Grimme, S. et al. A consistent and accurate ab initio parametrization of density functional dispersion correction (DFT-D) for the 94 elements H-Pu. *J. Chem. Phys.* **132**, 154104 (2010).
66. Nørskov, J. K. et al. Origin of the overpotential for oxygen reduction at a fuel-cell cathode. *J. Phys. Chem. B* **108**, 17886–17892 (2004).
67. Man, I. C. et al. Universality in oxygen evolution electrocatalysis on oxide surfaces. *ChemCatChem* **3**, 1159–1165 (2011).

## Acknowledgements

We are grateful to the National Natural Science Foundation of China (22471192, 92161103, 22071180, 22022108 and 92461314). The XAS collection was performed at beamline 10-BM, supported by the Materials Research Collaborative Access Team (MRCAT). Use of the Advanced Photon Source, an Office of Science User Facility operated for the U.S. Department of Energy (DOE) Office of Science by Argonne National Laboratory, was supported by the DOE under Contract DE-AC02-06CH11357. We are grateful of Dr. Tao Liu and Qiang Liu from State Key Laboratory of Fine Chemicals, Dalian University of Technology for the zero-field $^{57}$Fe Mössbauer spectra data collection and fitting.

## Author contributions

Z.-M.Z. and H.-Q.Y. conceived and designed the project. H.W. and Z.W. prepared the samples and performed the initial discovery and optimization of reaction conditions. Y.F. and W.L. collected, fitted and analyzed the XAS data. G.-L.Z. and W.Z. conducted DFT calculations and analyzed the calculation results. H.W., H.-Q.Y., S.Y., Z.W., W.L. and Z.-M.Z. analyzed the results and co-organized the manuscript. S.Y., Z.-M.Z., T.-B.L. and W.L. revised the manuscript. All the authors discussed the results and commented on the manuscript.

## Competing interests

The authors declare no competing interests.

## Additional information

**Supplementary information** The online version contains supplementary material available at https://doi.org/10.1038/s41467-025-61129-x.

**Correspondence** and requests for materials should be addressed to Hua-Qing Yin, Wenbin Lin or Zhi-Ming Zhang.

**Peer review information** *Nature Communications* thanks Yakubu Alli, and the other, anonymous, reviewer(s) for their contribution to the peer review of this work. A peer review file is available.